Astronomy & Astrophysics manuscript no. ms
November 6, 2021

Observations of solar chromospheric oscillations at 3 mm with ALMA

S. Patsourakos[1], C.E. Alissandrakis[1], A. Nindos[1], and T. S. Bastian[2]

[1] Physics Department, University of Ioannina, Ioannina GR-45110, Greece
e-mail: spatsour@uoi.gr
[2] National Radio Astronomy Observatory, 520 Edgemont Road, Charlottesville VA 22903, USA

Received: Accepted:

ABSTRACT

Aims. To study spatially-resolved chromospheric oscillations of the quiet Sun in the mm-domain at a resolution of a few arcsec, typically 2.4″×4.5″.
Methods. We used Atacama Large millimeter and sub-millimeter Array (ALMA) time-series of interferometric observations of the quiet Sun obtained at 3 mm with a 2-s cadence and a spatial resolution of a few arcsec. The observations were performed on March 16, 2017 and seven 80″×80″fields-of-view going from disk center to limb were covered, each one observed for 10 min, therefore limiting the frequency resolution of the power spectra to 1.7 mHz. For each field of view, masks for cell and network were derived, and the averaged power spectral densities (PSDs) for the entire field of view, cell and network were computed. The resulting power spectra were fitted with an analytical function in order to derive the frequency and the root-mean-square (rms) power associated with the peaks. The same analysis, over the same fields of view and for the same intervals, was performed for simultaneous Atmospheric Imaging Assembly (AIA) image sequences in 1600 Å.
Results. Spatially-resolved chromospheric oscillations at 3 mm, with frequencies of 4.2 ± 1.7 mHz are observed in the quiet Sun, in both cell and network. The coherence length-scale of the oscillations is commensurate with the spatial resolution of our ALMA observations. Brightness-temperature fluctuations in individual pixels could reach up to a few hundred K, while the spatially averaged power spectral densities yield rms in the range ≈ 55-75 K, i.e., up to ≈ 1 % of the averaged brightness temperatures and exhibit a moderate increase towards the limb. For AIA 1600 Å the oscillation frequency is 3.7 ± 1.7 mHz. The relative rms is up to 6% of the background intensity, with a weak increase towards disk center (cell, average). ALMA 3 mm time-series lag AIA 1600 Å by ≈ 100 s, which corresponds to a formation-height difference of ≈ 1200 km, representing a novel determination of this important parameter.
Conclusions. The ALMA oscillations that we detected exhibit higher amplitudes than those derived from the lower (≈ 10″) resolution observations at 3.5 mm by White et al. (2006). Chromospheric oscillations are, therefore, not fully resolved at the length-scale of the chromospheric network, and possibly not even at the spatial resolution of our ALMA observations. Any study of transient brightenings in the mm-domain should take into account the oscillations.

Key words. Sun: radio radiation – Sun: quiet – Sun: atmosphere – Sun: chromosphere

1. Introduction

Oscillation and wave phenomena are ubiquitous throughout the solar atmosphere (see the reviews by Tsiropoula et al. 2012 and Jess et al. 2012 and the references therein). Chromospheric oscillations with periods between 3-5 minutes could represent the intrusions of the photospheric p-modes (Leighton et al. 1962) into the chromosphere (e.g., Jefferies et al. 2006). However, given the inhomogeneous nature of the chromosphere, along with the transition between plasma-dominated dynamics (i.e., high plasma β) in the photosphere to magnetic-dominated dynamics (i.e., low plasma β) in the chromosphere, a complex picture of wave and oscillation phenomena has been established for the chromosphere which includes mode conversions, reflections, interferences, and shocks. (e.g., Wedemeyer-Böhm et al. 2009). The importance of chomospheric oscillations and waves is manifold as they could supply a means to heat plasmas and a probe of atmospheric conditions, including the magnetic field.

Almost all observations of chromospheric oscillations in either intensity or Doppler shifts have been performed in the visible or the extreme ultraviolet (EUV). The derivation of physical parameters from such observations, relies on complex diagnostics with complicated physical effects such as departures from local thermodynamic equilibrium, partial and time-dependent ionization being highly relevant (e.g., Leenaarts et al. 2013).

On the other hand, observations of free-free emissions in the radio domain are devoid of the complications described above, and in addition, as per Rayleigh-Jeans law, the observed brightness temperatures are directly (linearly) linked to the plasma temperature (e.g., Shibasaki et al. 2011). Given now the standard variation of temperature and density with height in the solar atmosphere, the chromosphere is probed in mm-wavelengths by the above mechanism.

Unfortunately, even moderate spatial resolution observations of the solar chromosphere in the mm-domain are rather scant. A notable exception are the BIMA observations of White et al. (2006) and Loukitcheva et al. (2006). Their BIMA observations at 3.5 mm covered both quiet Sun (QS) and active region targets with fields of view truncated to 72″. The spatial resolution of ≈ 10″ of the BIMA observations did not allow a complete separation between network and cell elements, and the above authors had to use a Ca II spectroheliogram to achieve this task. Therefore, some mixing between cell and network elements was un-

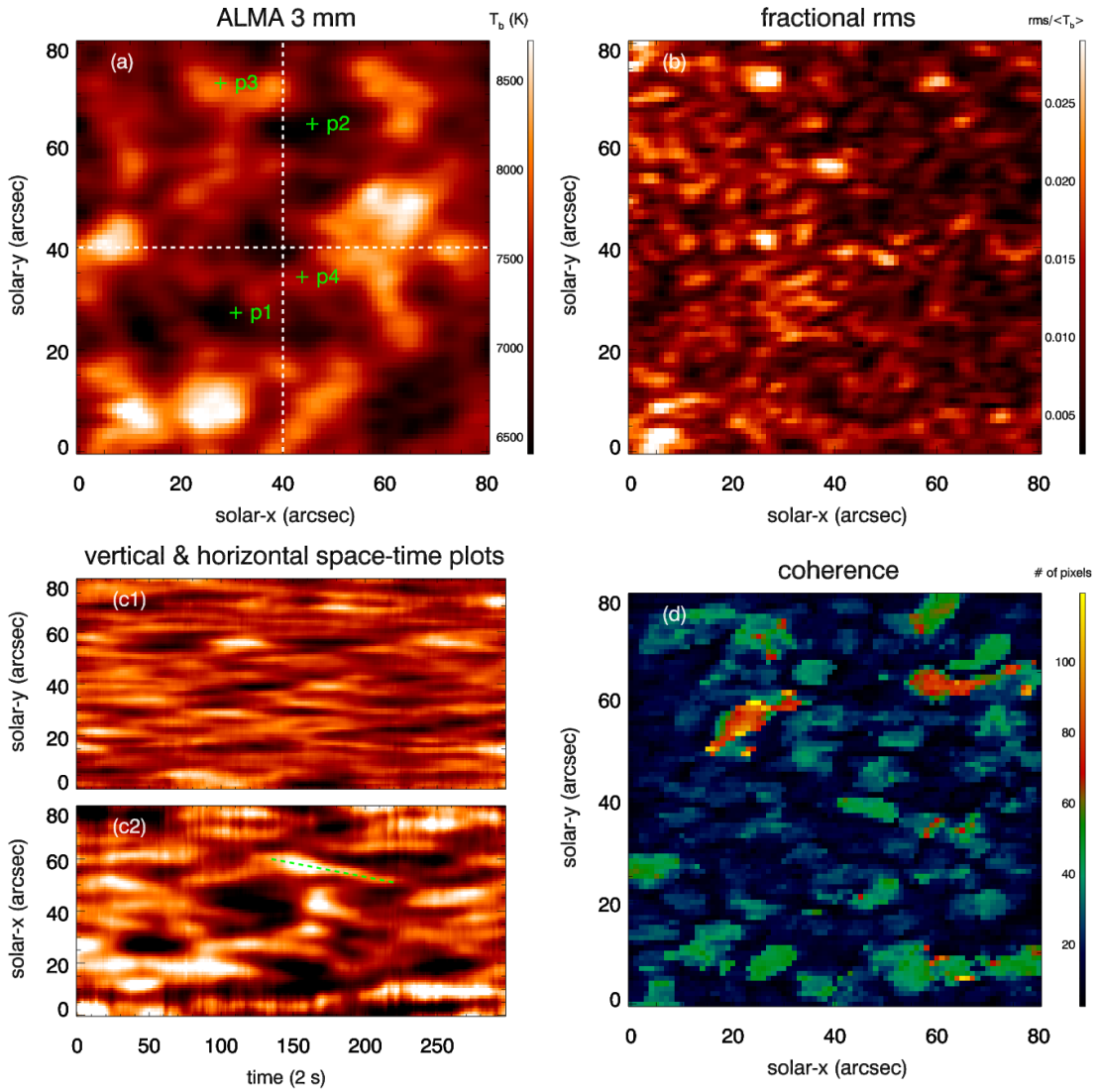

Fig. 1. Summary plots for target 5. (a): temporally-averaged ALMA 3-mm image, (with p1-p4 we show the four pixels used in Figure 2); (b): fractional rms of T_b; (c): space-time plots of T_b corresponding to a vertical (upper panel) and horizontal (lower panel) cut through the center of image of (a); from each light-curve its temporal average was subtracted and the color-scale was saturated to differences of ± 200 K: (due to the non-circular ALMA beam the resolution in the vertical direction is inferior to that in the horizontal direction: see Table-1 of Nindos et al. 2018); (d) coherence map displaying the number of pixels in the neighborhood of each pixel with linear correlation coefficient of the corresponding light-curves of at least 0.7. Images are oriented with celestial north up.

avoidable. White et al. (2006) reported p-mode oscillations with periods of 3-5 minutes, and even longer period oscillations for the case of the network.

The commencement of solar observations with ALMA in 2015 marked a new and exciting era of chromospheric investigations. This is because of the superior spatial resolution and sensitivity that ALMA is offering. In particular, the interferometric ALMA observations reach spatial resolution of a few arcsec or less, a significant improvement over the previous observation in the mm-domain, which indeed starts to somehow bridge the gap with commensurate observations in the infrared, optical and EUV wavelengths (for a review of the ALMA capabilities in solar observing see Wedemeyer et al. 2016). Observations of the quiet Sun with ALMA include Alissandrakis et al. (2017); Bastian, et al. (2017); Shimojo et al. (2017); White et al. (2017); Braja et al. (2018); Nindos et al. (2018); Yokoyama et al. (2018); Jafarzadeh et al.(2019); Loukitcheva et al. (2019); Molnar et al. (2019); Selhorst, et al. (2019).

We hereby present the first ALMA observations of quiet Sun chromospheric oscillations at 3 mm. Our observations allow for the first time to study chromospheric oscillations in the mm-domain with a spatial resolution adequate to clearly distinguish between cell and network and, in addition, to follow the center-to-limb variation of their properties, including their frequency and relative amplitude. Moreover, we compare with AIA (Lemen et al. 2011) observations taken in its 1600 Å channel, and derive temporal lags between the ALMA and AIA oscillations. In Section 2 we discuss our observations and their analysis; Section 3 contains the results of our analysis and we conclude in Section 4 with a summary and discussion of our results.

2. Observations and data analysis

We used ALMA observations of the quiet Sun described by Nindos et al. (2018). In short, seven 120" circular fields of view (targets) were observed at 3 mm (100 GHz) on March 16, 2017. The

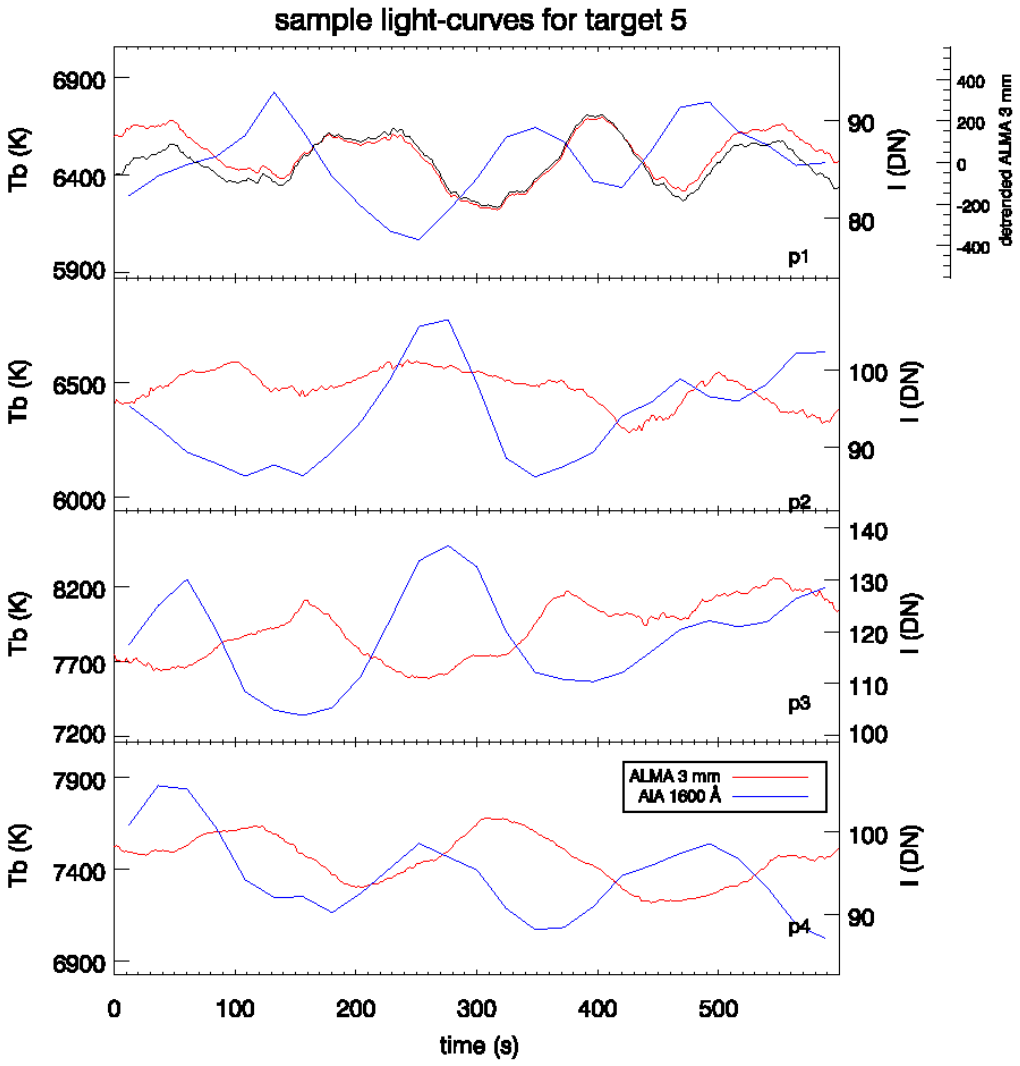

Fig. 2. ALMA 3 mm (red curve) and AIA 1600 Å (blue curve) light-curves for the four selected pixels shown in Figure 1. The black curve of the upper panel shows the ALMA light curve after the subtraction of a 3rd-degree polynomial fit.

ALMA targets, numbered from 1 to 7, correspond to μ=[0.16, 0.34, 0.52, 0.72, 0.82, 0.92, 1] along a line at a position angle of 135°, therefore supplying a center-to-limb coverage (see Table 1 of Nindos et al., 2018). Since the field of view (FoV) of target 1 included off-limb locations, we refrained from using it for further analysis, therefore limiting ourselves to targets 2-7. Each target was observed for 10 minutes with a 2-s cadence. The resulting ALMA images have 1″ pixels; the spatial resolution, as resulting from the beam size, for all targets was 2.4″×4.5″, with the exception of target 7 where the resolution was 2.3″×8.1″. The ALMA images were already corrected for the (small) effect of solar rotation. More details regarding the reduction of the ALMA data can be found in Nindos et al. (2018).

We extracted a 80″×80″region from the original 120″ diameter FoV at the center of each target to avoid artifacts resulting from the primary beam correction towards the edges of each FoV. Given that the mean diameter of supergranulation cells is around 20-30″, our truncated FoVs encompass a significant number of supergranulation cells to allow for the determination of meaningful statistics of the quiet Sun.

We also analyzed AIA images at 1600 and 304 Å, convolved with the ALMA resolution, both for purpose of comparison and as a check of our 3 mm computations. Note here that Howe et al. (2012), from the analysis of QS oscillations in the 1600 Å and 1700 Å channels of AIA, showed that the two emissions are formed at similar heights, which suggests that the 1600 Å channel emission is mainly of chromospheric (i.e., continuum) and not transition region (i.e., C IV line) origin.

We selected the same regions and the same time intervals used for the ALMA analysis. The main difference is that the cadence of the AIA images is lower, 12 s and 24 s for 304 Å and 1600 Å respectively. This limits the highest PSD frequency to 42 mHz and 24 mHz respectively, compared to 250 mHz of the ALMA data set; all three values are though well above the p-mode frequency of ∼ 3 mHz. The frequency resolution of all three data sets, determined by the duration of the time series, is 1.7 mHz. The AIA images were first corrected for differential rotation. Next, the AIA and ALMA were co-aligned by first considering the celestial orientation of the ALMA images and then cross-correlating the corresponding temporally-averaged images for each target.

An example of our ALMA observations can be found in Fig. 1, and refers to target 5 ($\mu = 0.82$). In panel (a) we display the temporally-averaged ALMA 3 mm image over the corresponding 10-min interval. Thanks to the spatial resolution of our ALMA observations, the differentiation between cell and network is obvious and several network elements could be readily discerned. In panel (b) of Fig. 1 we display a fractional rms map which contains the fraction of the rms of the light-curve at each pixel with the corresponding temporal average of T_b ($< Tb >$). Prior to the calculation of the rms for each light curve, a 3rd-degree polynomial fitting was subtracted. Weak fluctuations of T_b not exceeding few percent can be observed throughout the FoV; the mean value is around 1 %. We are not though able to observe a significant correspondence between the temporally-averaged image of panel (a) and the fractional variability map of panel (b) (linear correlation coefficient of 0.12).

Panel (c) contains space-time plots of T_b corresponding to a vertical (upper plot) and a horizontal (lower plot) cut through the center of the image of panel (a). To enhance visibility of oscillatory behavior we subtracted the corresponding temporal average from the light curve at each location along the cuts. T_b-oscillations correspond to alternating black and white patches along the time axis at a given location. The amplitude of the oscillations at individual pixels could reach values of ≈ 350 K. Such patterns are common and cover both cell and network locations. One to two periods are observed. Patches showing oscillatory behavior span several pixels along the spatial direction and correspond to scales of up $\approx 10''$. This suggests that the oscillations exhibit a degree of spatial coherence. We also note the occasional appearance of bright lanes, inclined with respect to the spatial axis (e.g., corresponding to the dashed green line in the lower plot of panel (c)). Such lanes are indicative of an apparent motion of a T_b front. The analysis of such fronts deserves a separate study.

In addition, in Figure 2 we supply sample light-curves for four pixels for target 5, indicated as p1-p4 in Figure 1a, with the first two corresponding to cell and the other two to network. Again, the oscillatory behavior is rather obvious. Indeed p1 shows higher frequency oscillations.

We then investigated in more detail the spatial coherence of the T_b fluctuations as follows. We first calculated the cross-correlation coefficient between the light curve of each pixel of the FoV and the light curves of the remaining pixels. Prior to the calculation of the cross correlation we subtracted a 3rd-degree polynomial fitting from each light curve. Next, initiating a region-growing algorithm at each pixel, we determined clusters of pixels with cross-correlation coefficient above 0.7 and counted the number of pixels per cluster. This pixel count is displayed in the coherence map of panel (d) of Fig. 1. Adjacent pixels with high correlations of their light-curves imply coherent (in-phase) T_b fluctuations (oscillations). Again, from the inspection of the fractional variability map of panel (b), we cannot observe any strong correspondence between the coherence map and the temporally-averaged image of panel (a) (linear correlation coefficient of 0.1). The average number of high-correlation pixels in the vicinity of a given pixel in the FoV is ≈ 20. This corresponds to a square with a side of $\approx 4''$, which is comparable with the ALMA spatial resolution. Therefore, this sets an upper limit on the spatial coherence of QS fluctuations we observe. This number exhibited a small variation from 18-25 for all considered targets, with the exception of target 7 for which it was equal to 45, apparently due to the lower resolution of the ALMA images for this target. Panels (b) and (d) of Fig. 1 exhibit some similarities; this comes to no surprise since both supply different and complementary means to look into the fluctuations in the light-curves.

Note here that inspection of 2D maps of the PSDs integrated over selected frequency ranges (e.g., covering the p-mode domain) do not reveal any correspondence with structures observed in the original ALMA images, at variance of structures such as the "shadows" and "halos" observed in relation to chromospheric oscillations in other wavelengths (e.g., review of Tsiropoula et al. 2012). This lack is possibly due to the small duration of our ALMA observations per target (i.e., ≈ 10 min).

In order to determine the characteristics (e.g., amplitude, frequency) of the p-mode oscillations we performed a series of steps described below.

2.1. Cell-Network Segregation

After building the temporal average of all images per target, using the truncated-FoV images discussed above, we submitted the resulting average images to the masking procedure described in Nindos et al. (2018). This essentially calculates a low-order (i.e., second-degree) 2D polynomial fitting of the average image, which is meant to represent the large-scale structure of the corresponding scene. Pixels with values smaller (larger) than these of the mask are tagged as cell (network) pixels. As also discussed in Nindos et al. (2018), our employed method of separating network-cell is by no means unique; it though leads to satisfactory results as judged by visual inspection of the resulting masks and the actual average images.

2.2. Calculation of Power Spectral Density

Next, the light-curves of each pixel were submitted to a Fourier analysis to derive the corresponding Power Spectral Density (PSD). Having N evenly sampled points in a light-curve x_n ($n = 1, 2, .., N$) the corresponding PSD is given by:

$$\mathrm{PSD}(f_j) = \frac{2N}{fs}|\tilde{x}_j|^2, \quad (1)$$

with $j = 1, 2, .., N/2$, $\tilde{x}$ is the discrete Fourier transform of x_n and fs is equal to the sampling frequency. In our application, x_n corresponds to the observed T_b time-series.

From each light curve we first subtracted a 3rd-degree polynomial fitting to remove long-term trends from the data (see also White et al. 2006). This essentially leads to zero mean value of the resulting light curves and therefore quenches the zero frequency (DC term) in the corresponding power spectra. Moreover, it eliminates the non-periodic, slow-varying background from the light curves, leaving only temporal fluctuations around the mean level. Therefore, each light curve will contribute to the spatially-averaged PSDs according only to the amplitude of the corresponding fluctuations and not of the intrinsic brightness of the spatial pixel under consideration. An example of this procedure is given in the upper panel of Fig. 2, where the red curve corresponds to the ALMA 3 mm light-curve for pixel p1 of Fig. 1c, while the black curve corresponds to the result of the subtraction of the 3rd degree polynomial fitting from the red curve.

We then calculated the PSDs for every pixel in the FoV and averaged over the entire FoV, as well as the cell and network using the masks described above. Averaging PSDs of individual pixels, rather than first calculating spatially-averaged light curves and then calculating the corresponding PSDs, guarantees that oscillatory patterns in pixels which are out-of-phase are not smeared out. The PSDs both before and after the subtraction of

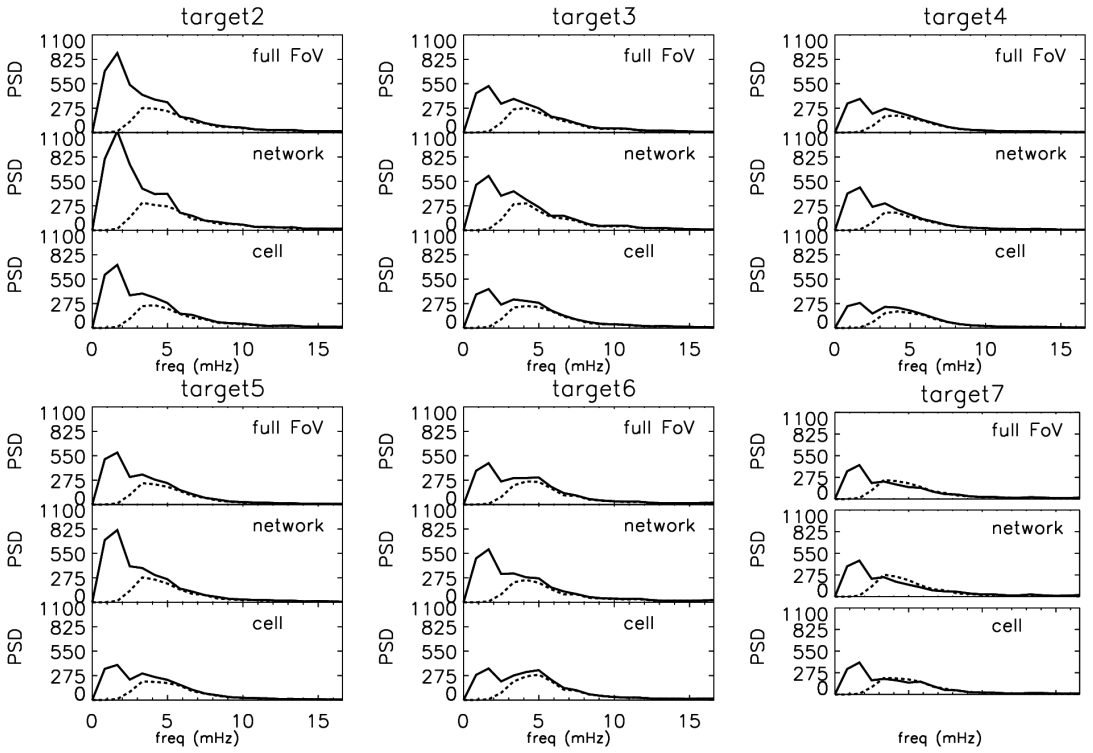

Fig. 3. Power spectra from full FoV (first row), network (second row) and cell (third row) for targets 2-7. Solid lines correspond to spectra computed after the subtraction of the average from the light-curves of individual pixels, dashed lines show the spectra computed after the subtraction of a 3rd-degree polynomial fit. All spectra have been scaled by a factor equal to 4815 K^2/Hz.

the 3rd degree polynomial fittings are displayed in Fig. 3 and will be discussed in detail in Section 3.

2.3. Fitting of spatially averaged power spectra

The spatially averaged PSDs were then fitted with the following function:

$$\mathrm{PSD}(f) = a_0 + a_1 f + a_2 \exp\left(-\frac{(\ln f - \ln a_3)^2}{2{a_4}^2}\right), \quad (2)$$

with $a_0 - a_4$ being the parameters of the fitting function. The fitting function of Equation 2 treats the observed PSDs as a sum of a linear function describing the background (noise) spectrum described by the terms a_0 and a_1, and with a log-normal (Gaussian of $\ln f$), describing the peak associated with chromospheric oscillations; a_2 is the oscillation amplitude, a_3 is the frequency at maximum power and a_4 is related to the width of the spectral peak. We note that both the amplitude and the width are determined by the frequency resolution of the time series rather than the properties of the p-modes, thus the physically meaningful quantities are the frequency at maximum power and the integral of the exponential term over frequency, which evaluates to

$$a_2 \int_0^\infty \exp\left(-\frac{(\ln f - \ln a_3)^2}{2{a_4}^2}\right) df = a_2 \sqrt{2\pi} a_4 \exp\left(\frac{a_4^2 + 2\ln(a_3)}{2}\right) \quad (3)$$

This represents the total power of the oscillations and is equal to the rms of their amplitude.

The choice of Equation 2 to fit the PSDs is by no means unique; however, as can be seen in Figs. 4 and 6, displaying the averaged PSDs for ALMA 3 mm and AIA 1600 Å ,respectively, it gives a good representation of the observed PSDs, and their peaks in particular, as required for our purposes to characterize the observed chromospheric oscillations. Log-normal fittings of peaks in PSDs have been employed in other investigations of oscillatory phenomena (e.g., Ireland et al. 2015; Morton et al. 2019). Regarding the choice of a linear function to describe the noise in the PSDs, hence implying a white-noise spectrum, it is well-known that the noise in solar PSDs could be represented by power-laws on several occasions/features (e.g., Ireland et al, 2015; Auchère et al. 2016). However, the short duration of the analyzed sequences per target (i.e., $\sim$ 10 min), does not allow to extend the PSDs to significantly lower frequencies than these corresponding to the p-mode regime so as to obtain a fair representation of the noise spectrum at both sides of the corresponding peaks. In addition, since we focus on narrow frequency windows around the peaks, a linear background is deemed as a reasonable choice. A final note regarding this point is in order: as can be seen by simple inspection of Figs. 4 and 6 the p-mode peaks stand significantly above the corresponding backgrounds. Therefore, it is reasonable to expect that the specifics of the employed background model will have a minor impact on the characteristics of the spectral peak fittings (e.g., amplitude). The fittings were performed in the frequency range of $\approx$ [0.008, 13.3] mHz, spanning essentially the spectral peaks and the adjacent background seen in Figs. 4 and 6.

3. Results

3.1. ALMA 3 mm

The spatially-averaged PSDs for the entire FoV, network and cell for all targets are displayed in Fig. 3. In addition to displaying PSDs resulting from the subtraction of a 3rd degree polynomial fitting from the original light curves (dashed lines

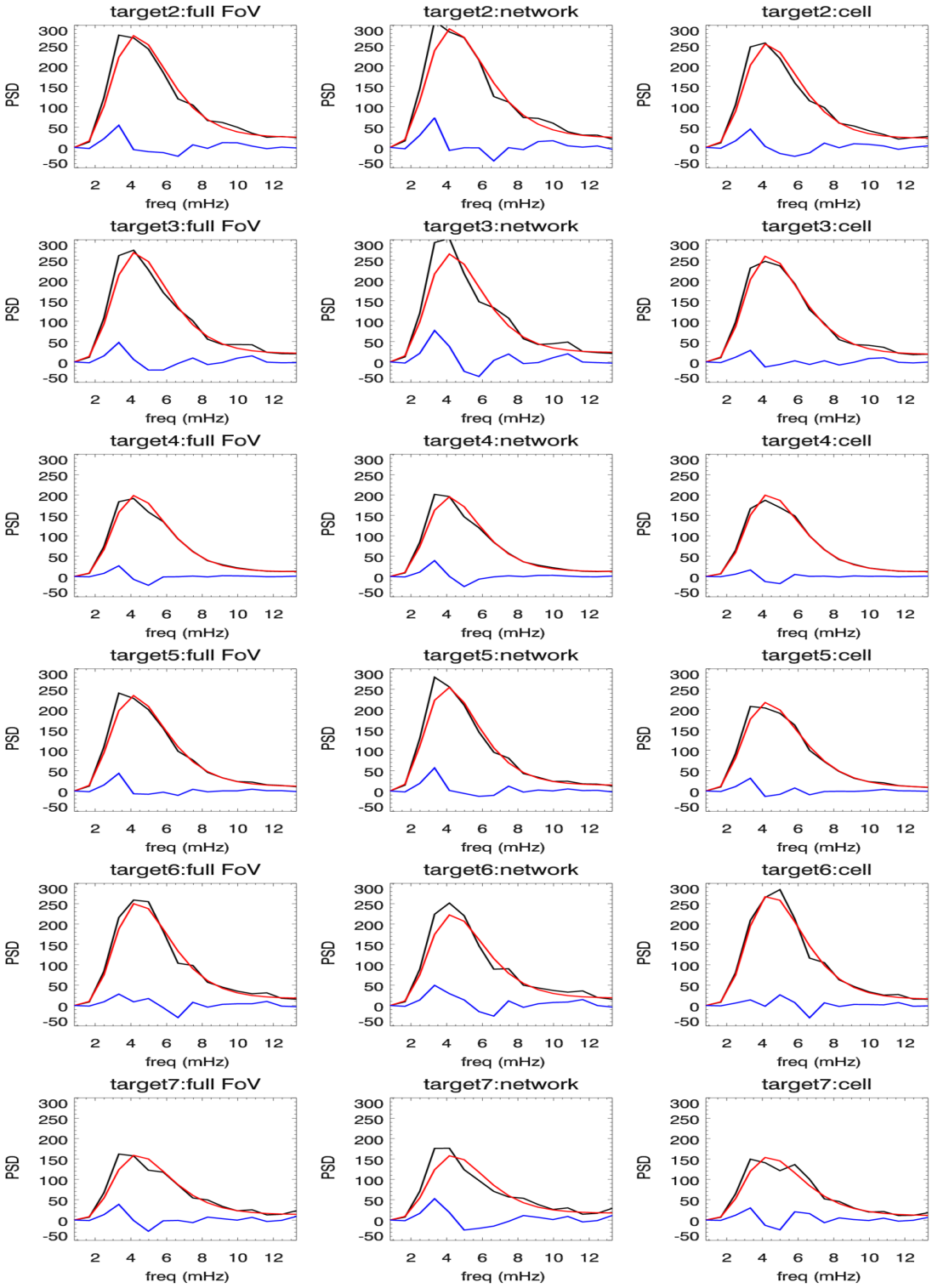

Fig. 4. Averaged ALMA 3-mm PSDs (black line) for the entire FoV, network and cell (first, second and third column, respectively) for targets 2-7 (top to bottom row); the corresponding fittings with Equation 2 are plotted with a red line and the residuals (observed PSDs - fittings) with a blue line. All PSDs have been scaled by a factor equal to 4815 K^2/Hz.

in Fig. 3; PSD_{poly}) as discussed above, we are also displaying PSDs (PSD_{av}) resulting from the subtraction of the light-curve average PSD_{av}) instead (solid lines in Fig. 3). We first note that only the PSD_{av} curves exhibit a low-frequency peak close to 0 corresponding to long-term trends in the original light curves; with an increase towards the limb. Such peaks do not show up in the PSD_{poly} curves as a result of the application of the polynomial fitting to the original light curves. On the other hand, both PSD_{poly} and PSD_{av} exhibit well-defined strong peaks in the p-mode range, i.e., ≈ 3-4 mHz with similar locations and amplitudes. Therefore, the identification of p-modes in our ALMA observations is robust. This conclusion, along with the discussed-above low-frequency peak in the PSD_{av} curves, which prevents a proper mapping of the p-mode peaks, led us to use the PSD_{poly}

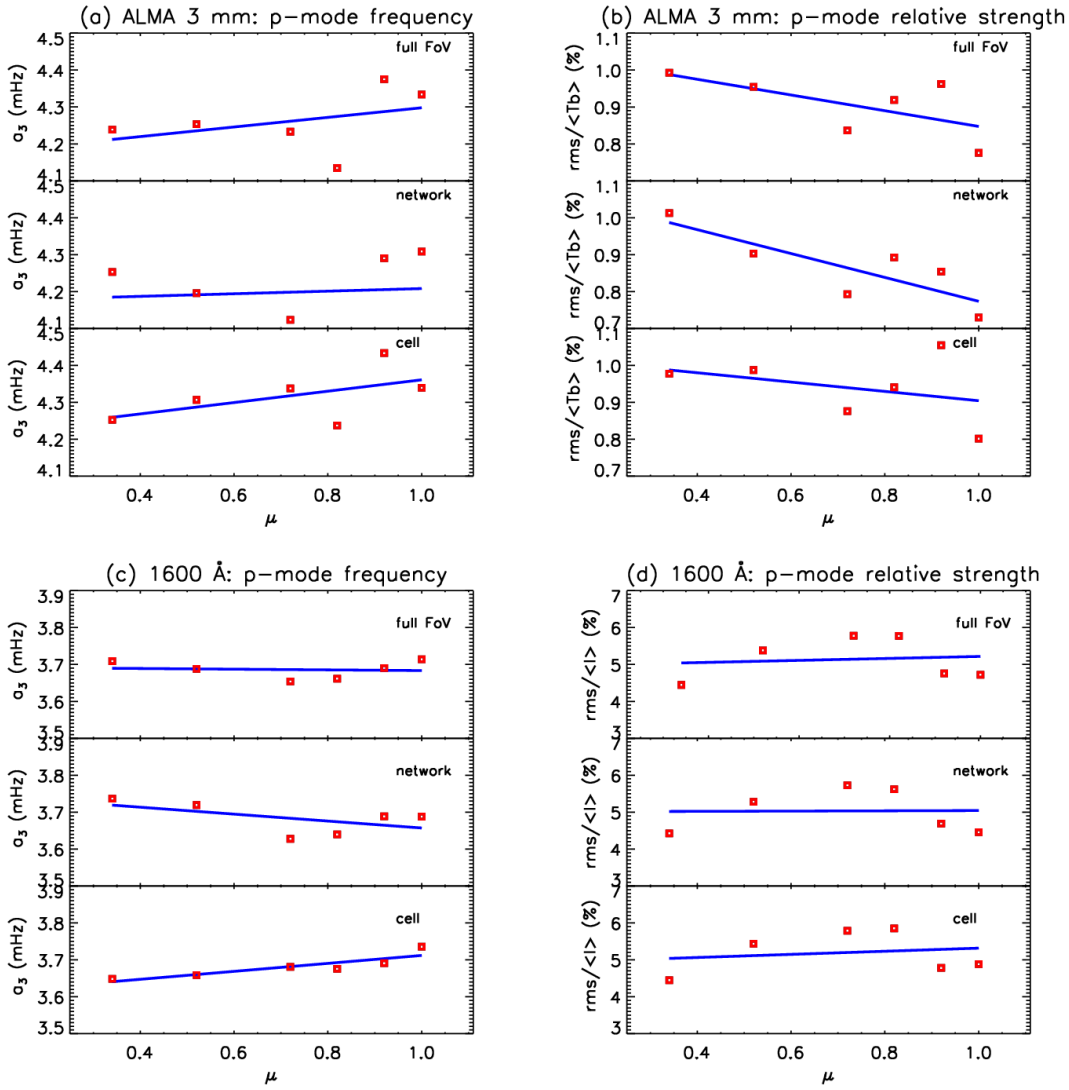

Fig. 5. ALMA 3 mm center-to-limb variation (red boxes) for: (a) p-mode frequency (i.e., a_3 in Equation 2), (b) p-mode relative strength, i.e., rms associated with p-mode/<Tb> (%). AIA 1600 Å center-to-limb variation (red boxes) for: (c) p-mode frequency (i.e., a_3 in Equation 2), (d) p-mode relative strength, i.e., rms associated with p-mode/$< I >$ (%). Blue lines correspond to linear fits of the corresponding measurements. In each panel, top, middle and bottom plots correspond to the entire FoV, network and cell, respectively.

curves for further analysis. Note here that experimentation with different degree polynomials (i.e., 1-4) showed that the higher the degree of the polynomial, the smaller the amplitude of the peak around the p-mode domain. Therefore, the derived p-mode rms amplitudes from the use of a 3rd degree polynomial fitting of the original light-curves could be seen as upper limits. Obviously, employing longer duration ALMA time-series will remedy some of the issues we encountered here. Finally, for frequencies above the p-mode range both PSD_{poly} and PSD_{av} are practically the same. Note here that although the duration of the time series is barely equal to twice the period of p-mode oscillations, the peak stands out clearly in the power spectra.

The resulting averaged PSDs for the full FoV, cell and network were then fitted with the function of Equation 2. From Fig. 4 we observe that the employed fitting function (red lines) does a good job at reproducing the observed PSDs (black lines) with residuals (blue lines) not exceeding ≈ 15%.

We finally plot in Fig. 5 the center-to-limb variation of the peak frequency (i.e., parameter a_3 of Equation 2; panel a) and the relative (%) rms of the p-modes (i.e., the ratio between the rms corresponding to the Gaussian part of Equation 2 as resulting from application of Equation 3 and the average T_b) for the entire FoV, cell and network. The corresponding values are tabulated in Table 1. From Fig. 5 we observe that the oscillation frequencies are ≈ 4.2 mHz (the moderate apparent increase towards the limb is within the frequency resolution); the oscillation rms is small (≈ 55-75 K), and conversely up to ≈ 1 % of the averaged T_b. It exhibits a moderate increase towards the limb. The peak frequency of the oscillations is somewhat larger in the cell compared to the network. We note, however, that frequency differences are considerably smaller than the 1.7 mHz frequency resolution of the PSD.

3.2. AIA 1600 and 304 Å

We degraded our AIA 1600 Å image sequences to the ALMA spatial resolution and submitted them to the same analysis as the ALMA data, discussed previously. p-mode oscillations are also present in 1600 Å light-curves as originally observed by TRACE

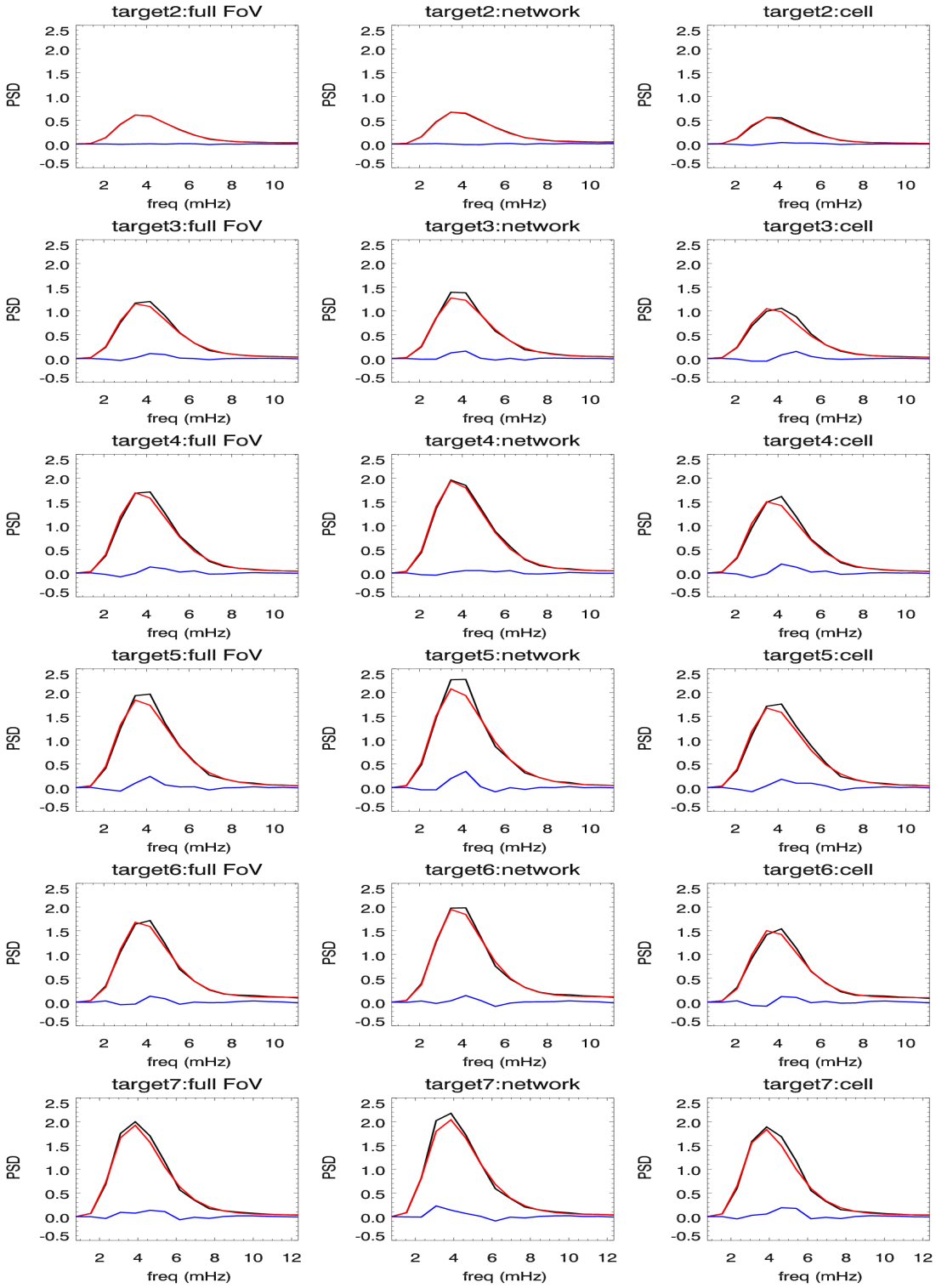

Fig. 6. Averaged AIA 1600 Å PSDs (black line) for the entire FoV, network and cell (first, second and third column) for targets 2-7 (top to bottom row); the corresponding fittings with Equation 2 are plotted with a red line and the residuals (observed PSDs - fittings) with a blue line. All PSDs have been scaled by a factor equal to 5760 DN/s^2/Hz; DN correspond to the digital numbers recorded by AIA.

(e.g., Krijger et al. 2001), and such periodic behavior is omnipresent within the observed fields of view. Moreover, the corresponding light-curves were smoother than those we obtained for ALMA.

The spatially averaged PSDs for the full FoV, cell and network as well as the corresponding fittings with the function of Equation 1 are displayed in Fig. 6. As for the ALMA PSDs, we note the existence of a strong peak in the p-mode domain in each PSD. In addition, the fittings of the PSDs (black lines) with Equation 1 (red lines) do a good job, and lead to residuals (blue lines) which do not exceed ≈ 10 %.

The peak frequency (i.e., parameter a_3 of Equation 2) and the relative (%) rms of the p-modes (i.e., the ratio between the rms corresponding the Gaussian part of Equation 2 as resulting from

Table 1. ALMA 3 mm: center-to-limb variation variation of oscillation parameters.

	μ					
	1.00	0.92	0.82	0.72	0.52	0.34
			Full FoV			
a_3 (mHz)	4.3	4.3	4.1	4.2	4.2	4.2
rms (K)	56	70	67	61	71	72
rms/$< T_b >$	0.78	0.96	0.92	0.84	0.95	0.99
			Network			
a_3 (mHz)	4.3	4.2	4.0	4.1	4.2	4.2
rms (K)	55	65	68	60	70	77
rms/$< T_b >$	0.73	0.85	0.89	0.79	0.90	1.01
			Cell			
a_3 (mHz)	4.3	4.4	4.2	4.3	4.3	4.2
rms (K)	55	73	66	61	71	69
rms/$< T_b >$	0.80	1.05	0.94	0.88	0.99	0.98

Table 2. AIA 1600 Å : center-to-limb variation variation of oscillation parameters.

	μ					
	1.00	0.92	0.82	0.72	0.52	0.34
			Full FoV			
a_3 (mHz)	3.7	3.6	3.6	3.6	3.6	3.7
rms (DN)	5.7	5.3	5.8	5.5	4.6	3.3
rms/$< I >$	4.7	4.8	5.8	5.9	5.4	4.5
			Network			
a_3 (mHz)	3.6	3.6	3.6	3.6	3.7	3.7
rms (DN)	5.9	5.7	6.2	5.9	4.8	3.5
rms/$< I >$	4.5	4.7	5.6	5.7	5.3	4.4
			Cell			
a_3 (mHz)	3.7	3.6	3.6	3.68	3.6	3.6
rms (DN)	5.5	5.0	5.6	5.2	4.3	3.1
rms/$< I >$	4.9	4.8	5.9	5.8	5.4	4.5

the application of Equation 3) and the average recorded intensity ($< I >$) are plotted in panels (c) and (d) of Fig. 5 for the entire FoV, cell and network. The corresponding values are tabulated in Table 2. From Fig. 5 we observe that the peak frequency is ≈ 3.6 mHz with moderate increase (decrease) towards disk center and cell (network) within though the limit set by the frequency resolution of the obervations. The relative rms is up to 6% with a weak increase towards disk center (cell, average).

Inspection of the corresponding 304 Å data showed that the light-curves of the bulk of individual pixels were rather noisy and it was hard to infer periodic behavior. On the other hand, only a few pixels per target, with higher signal-to-noise ratio, showed oscillatory patterns. Since, (i) we are interested into oscillations characterizing extended, and thus representative, areas over the observed FoVs, and (ii) we used the AIA data for mainly supplying context to our ALMA oscillations we refrain from further discussion of the 304 Å data. Extended temporal sequences as well as spatial binning would certainly bring up better the oscillations in 304 Å something which, as discussed above, is beyond the scope our study.

3.3. Time-lag analysis

We finally performed a cross-correlation analysis of co-spatial AIA 1600 Å and ALMA 3 mm light-curves in order to determine temporal lags between the two emissions. This would allow to trace the oscillations between two different layers in the solar atmosphere and to eventually provide an estimate of the difference between the formation heights of the two emissions.

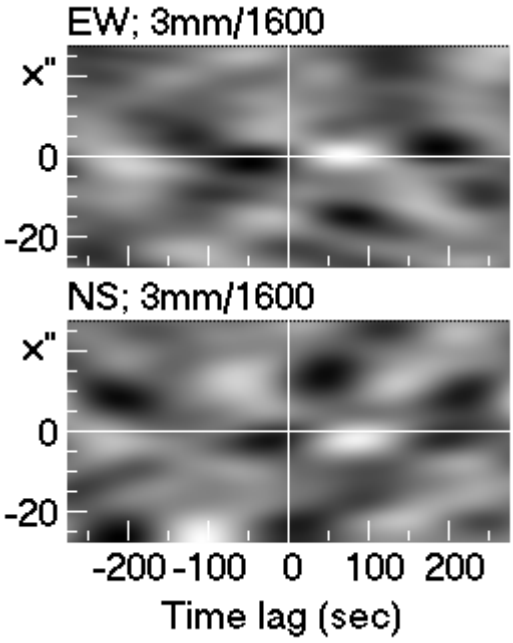

Fig. 7. 2D cross correlation maps of the AIA 1600 Å and ALMA 3 mm light-curves as a function of temporal lag and location along the employed horizontal (upper panel) and vertical (lower panel) cuts for target 5. White (black) correspond to strong positive (negative) correlation. The range of values is from -0.22 to 0.25.

Fig. 7 displays the cross-correlation function between the light-curves at 3 mm and 1600 Å, as a function of time lag, along two cuts (in the EW and NS direction) through a strong oscillating element in target 5. It shows strong peaks in the cross-correlation function at a lag of ≈ 80 s.

For a more detailed study, we computed the cross-correlation coefficient between the AIA 1600 Å and ALMA 3 mm light-curves averaged over 3″× 3″ macropixels, so that to decrease noise, and for an array of different temporal lags for all targets. For further analysis we only kept macropixels with maximum cross-correlation coefficients ≥ 0.7 so that to ensure strong correlation. A significant fraction of the total number of macro-pixels satisfied the above criterion ($\sim 0.25 - 0.45$). The optimal temporal lag was calculated from a parabolic fitting of the cross-correlation function around its peak.

Our results are shown in Fig. 8. There is no significant center-to-limb variation of the temporal lag between AIA 1600 Å and ALMA 3 mm, and its average value is ≈ 100 s, therefore suggesting that ALMA 3 mm lags AIA 1600 Å by ≈ 100 s ; this is slightly larger than the lag suggested by Fig. 7, which is within the dispersion of our measurements (error bars in Fig. 8). Given now that models and observations show that AIA 1600 Å forms below ALMA 3 mm (e.g., Shibasaki et al. 2011; Howe et al. 2012; Wedemeyer et al. 2016; Alissandrakis et al. 2017; Alissandrakis and Valentino 2019), our results imply *upward* propagating waves, consistent with p-mode propagation throughout the chromosphere. The decreasing relative rms of the p-mode oscillation in going from 1600 Å to ALMA 3 mm is also consistent with this assertion. We further note that Lindsey & Roel-

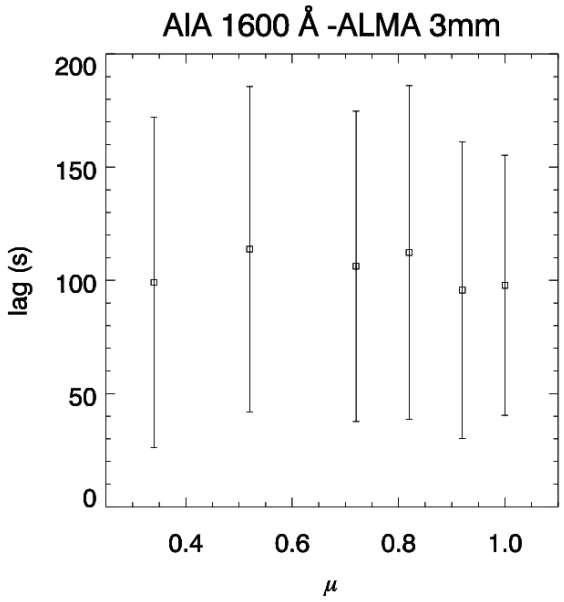

Fig. 8. Center-to-limb variation of the average lag (squares) between AIA 1600 Å and ALMA 3 mm light-curves for pixels corresponding to maximum cross-correlation ≥ 0.7. The vertical error bars specify the standard deviations of the corresponding distributions. Positive lag corresponds to AIA 1600 Å proceeding ALMA 3 mm.

lig (1987) reported a phase delay of 35° between oscillations at 0.8 mm and 0.35 mm in the frequency range of 3-4 mHz, which corresponds to a time lag of ∼ 28 s.

The validity of the above result might be questioned on the basis of the fact that the measured peak frequencies of the ALMA 3 mm and AIA 1600 Å oscillations are different, ≈ 4.2 and 3.6 mHz, respectively; this would lead to a lag of monochromatic oscillations with the same initial phase, so that, after some time, one oscillation would overtake the other. However, this possibility can be rather safely excluded, given the properties of the observed PSDs (e.g., Figures 3 and 4; Tables 1 and 2). Namely, the difference between the ALMA 3 mm and AIA 1600 Å oscillation frequencies is only 0.5 mHz, or about 30% of the frequency resolution of our observations (i.e., 1.7 mHz).

In addition, the observed oscillations are not monochromatic; they are much broader than the frequency difference, with FWHM of ≈ 4.5 mHz for ALMA 3 mm and somehow smaller for AIA 1600 Å in all targets. Both these facts imply that, within the limitation of the ALMA observations, differences between the power spectra of the two data sets are indistinguishable.

Moreover, if anything, the slightly higher ALMA oscillation frequency compared to AIA 1600,Å would eventually lead to AIA 1600 Å lagging ALMA 3 mm, rather preceding it, as our analysis suggests.

We may thus safely conclude that the time lag is real. Before interpreting the lag in terms of a height difference, a discussion on the dependence of the ALMA and AIA emissions on plasma parameters is warranted. The fact that the ALMA 3 mm images exhibit similar morphology as the AIA 1600 Å images (see Fig. 1 of Nindos et al. 2018), strongly suggests that the two emissions have similar dependencies on physical parameters; this is quantified by the high linear correlation coefficients between the ALMA 3 mm and AIA 1600 Å images taking values in the range of ≈ 0.6-0.8 for all targets.

We now supply a further discussion of the matter based on previous works. The mm emission, being optically thick, is directly related to plasma temperature, as per application of the Rayleigh-Jeans law. For the AIA 1600 Å channel the situation is more complicated. First note that the AIA 1600 Å channel intensities correspond to a band-pass few hundred Å wide around 1600 Å (Boerner et al. 2012). The emission in this spectral region is dominated by continuum emission via bound-free transitions from neutral Si, and from line transitions (e.g., Vernazza et al. 1981; Fossum and Carlsson 2005), and the bound-free absorption coefficient depends on the plasma temperature. Therefore, one would expect a relationship, albeit somehow complex due to radiative transfer complications, including non-LTE effects, and the non-linear character of the Planck function, between local plasma temperature and UV contiuum intensities. Indeed, detailed 1D non-LTE radiation hydrodynamic simulations of broad-band acoustic waves in the lower solar atmosphere, with frequencies covering these of our observations, showed that there exist heights where the local plasma temperature is correlated with the corresponding 1600 Å TRACE channel intensity (Fossum and Carlsson 2005). In addition, 3D non-LTE radiation hydrodynamic simulations of waves in the lower solar atmosphere by Wedemeyer et al. (2004), showed a decent correlation between a temperature slice at 500 km, i.e., within the range of formation heights of 1600 Å discussed below, and the corresponding 1600 Å intensity (check panels c and h of Figure 2 Wedemeyer et al. (2004)). In summary, we conclude that the intensities of both analyzed emissions depend primarily on temperature, although the details of on the exact dependence and its properties are far more obscure in the case of 1600 Å.

Assuming now that the observed p-mode oscillations in ALMA 3 mm and AIA 1600 Å are upward-propagating sound waves traveling at a speed of ≈ 12 kms^{-1} (i.e., corresponding to a temperature of 7000 K), and for the average temporal lag of ≈ 100 s between the two emissions we derived above, we find a height-separation of ≈ 1200 km between the formation layers of ALMA 3 mm and AIA 1600 Å. Our findings regarding the height-separation between the ALMA 3 mm and AIA 1600 Å formation layers are consistent with related observational and modeling work. Empirical modeling of the solar atmosphere indicates that 1600 Å forms at a height of ≈ 500-750 km (Shibasaki et al. 2011), whereas, analysis of TRACE observations of the 1999 Mercury transit showed a peak height of 500 km and a limb height of 1200 km (Alissandrakis and Valentino 2019). Radiation-hydrodynamics modeling of a broad-band spectrum of acoustic waves yields a formation height of the 1600 Å channel of TRACE, with similar wavelength response to the corresponding AIA channel, of 430 ± 185 km (Fossum and Carlsson 2005). Regarding ALMA 3 mm, empirical models show a formation range of ≈ 500 − 1500 km (Wedemeyer et al. 2016) and ≈ 1500 − 1800 km (Molnar et al. 2019); the center-to-limb variation ALMA study of Alissandrakis et al. (2017) suggest a range 980-1990 km.

4. Summary and conclusions

We performed the first study of chromospheric oscillations in the mm-domain with ALMA with a resolution of a few arcsec. Our main findings are summarized as following:

– p-mode oscillations at 3 mm are omnipresent in both network and cell with frequencies of 4.2 ± 1.7 mHz (periods 240 ± 80 s).

- Oscillation amplitudes of up to a few hundred K at individual pixels can be found.
- The spatially-averaged rms amplitude of oscillations is small (≈ 1 % of the average brightness temperature) and exhibits a moderate center-to-limb increase.
- Within the limits of our spectral resolution of 1.7 mHz, we did not find any significant differences in peak frequency between network and cell interior and for different positions from the center of the solar disk to the limb.
- Our analysis of simultaneous AIA 1600 Å images gave p-mode oscillations with similar frequencies, but stronger by a factor of ~ 6.
- ALMA 3 mm lags AIA 1600 Å by ~ 100 s; assuming upward propagating sound waves, and asserting that the emission intensities depend primarily on temperature in both wavelengths, this translates to a formation height difference of $\approx$ 1200 km.

Comparing our findings with the lower spatial resolution BIMA observations at 3.5 mm of White et al. (2006), we note that these authors found oscillations for both the cell and network with periods mainly in the domain 210-270 s and 270-330 s, close to the periods resulting from our analysis of the ALMA oscillations. However, given that their observing sequences had a duration of 30 min, there were also able to detect longer-period (> 5 minute) oscillations in the network. This we could not check with our ALMA observations, given that we were observing each target for only 10 minutes. White et al. (2006) also found rms brightness temperature amplitudes at individual pixels in the range 50-150 K, while the averaged QS time-series had an rms of 21 K. We found larger values for the oscillation amplitudes at individual pixels (up to a few hundred K), and a larger QS oscillation rms ($\approx$ 55-72 K), which are both suggesting that chromospheric oscillations in the mm-domain are not fully resolved at a resolution comparable to the length-scale of the network (i.e., $\approx 10''$). Given now that the spatial coherence of our ALMA observations has a length-scale comparable to the resolution of our ALMA observations implies that we are still not fully resolving individual oscillating elements. Higher spatial resolution ALMA are required in order to investigate this.

Before closing, we note that given the omnipresence of p-mode oscillations, and the significant oscillation amplitudes at individual pixels, any study of transient chromospheric brightenings needs to take them into account.

Acknowledgements. We would like to thank the referee for useful comments/suggestions. This work makes use of the following ALMA data: ADS/JAO.ALMA2016.1.00572.S. ALMA is a partnership of ESO (representing its member states), NSF (USA) and NINS (Japan), together with NRC (Canada) and NSC and ASIAA (Taiwan), and KASI (Republic of Korea), in cooperation with the Republic of Chile. The Joint ALMA Observatory is operated by ESO, AUI/NRAO and NAOJ.

References

Alissandrakis, C. E., Patsourakos, S., Nindos, A., & Bastian, T. S. 2017, A&A, 605, A78
Alissandrakis, C. E., & Valentino, A. 2019, Sol. Phys., 294, 96
Auchère, F., Froment, C., Bocchialini, K., Buchlin, E., & Solomon, J. 2016, ApJ, 825, 110
Bastian, T. S., Chintzoglou, G., De Pontieu, B., et al. 2017, ApJ, 845, L19
Boerner, P., Edwards, C., Lemen, J., et al. 2012, Sol. Phys., 275, 41
Brajša, R., Sudar, D., Benz, A. O., et al. 2018, A&A, 613, A17
Fossum, A., & Carlsson, M. 2005, ApJ, 625, 556
Howe, R., Jain, K., Bogart, R. S., et al. 2012, Sol. Phys., 281, 533
Ireland, J., McAteer, R. T. J., & Inglis, A. R. 2015, ApJ, 798, 1
Jafarzadeh, S., Wedemeyer, S., Szydlarski, M., et al. 2019, A&A, 622, A150
Jefferies, S. M., McIntosh, S. W., Armstrong, J. D., et al. 2006, ApJ, 648, L151
Jess, D. B., Morton, R. J., Verth, G., et al. 2015, Space Sci. Rev., 190, 103
Krijger, J. M., Rutten, R. J., Lites, B. W., et al. 2001, A&A, 379, 1052
Leenaarts, J., Pereira, T. M. D., Carlsson, M., et al. 2013, ApJ, 772, 90
Lemen, J. R., Title, A. M., Akin, D. J., et al. 2012, Sol. Phys., 275, 17
Leighton, R. B., Noyes, R. W., & Simon, G. W. 1962, ApJ, 135, 474
Lindsey, C., & Roellig, T. 1987, ApJ, 313, 877
Loukitcheva, M., Solanki, S. K., & White, S. 2006, A&A, 456, 713
Loukitcheva, M. A., White, S. M., & Solanki, S. K. 2019, ApJ, 877, L26
Molnar, M. E., Reardon, K. P., Chai, Y., et al. 2019, ApJ, 881, 99
Morton, R. J., Weberg, M. J., & McLaughlin, J. A. 2019, Nature Astronomy,
Nindos, A., Alissandrakis, C. E., Bastian, T. S., et al. 2018, A&A, 619, L6
Selhorst, C. L., Simões, P. J. A., Brajša, R., et al. 2019, ApJ, 871, 45
Shibasaki, K., Alissandrakis, C.E., & Pohjolainen, S. 2011, Sol. Phys., 273, 309
Shimojo, M., Bastian, T. S., Hales, A. S., et al. 2017, Sol. Phys., 292, 87
Tsiropoula, G., Tziotziou, K., Kontogiannis, I., et al. 2012, Space Sci. Rev. 169, 181
Vernazza, J. E., Avrett, E. H., & Loeser, R. 1981, ApJS, 45, 635
Yokoyama, T., Shimojo, M., Okamoto, T. J., et al. 2018, ApJ, 863, 96
Wedemeyer, S., Freytag, B., Steffen, M., et al. 2004, A&A, 414, 1121
Wedemeyer-Böhm, S., Lagg, A., & Nordlund, Å. 2009, Space Sci. Rev., 144, 317
Wedemeyer, S., Bastian, T., Brajša, R., et al. 2016, Space Sci. Rev., 200, 1
White, S. M., Loukitcheva, M., & Solanki, S. K. 2006, A&A, 456, 697
White, S. M., Iwai, K., Phillips, N. M., et al. 2017, Sol. Phys., 292, 88